Cross-Section Prediction Method for Proton Direct Ionization Induced Single Event Upset

K. Takeuchi, K. Sakamoto, Y. Tsuchiya, T. Kato, R. Nakamura, A. Takeyama, T. Makino, T. Ohshima, M. Hashimoto, *Senior Member, IEEE*, and H. Shindo

***Abstract*— This article proposes a method for predicting the cross section (XS) of single event upset (SEU) induced by proton direct ionization (PDI). The method is based on the physics-based model previously proposed for both bulk fin field-effect transistor (FinFET) static random access memories (SRAMs) and planar SRAMs under heavy ion (HI) irradiation. The method presented in this article predicts PDI XS for both 16-nm FinFET and 40-nm planar SRAMs below a few megaelectronvolt regime, thanks to the broad predictability of our XS model in linear energy transfer (LET) dependence. By calibrating the parameters through HI irradiation, our method enables the prediction of PDI SEU XS in SRAMs, which has not been analytically addressed in previous studies, and its validity has been verified.**

***Index Terms*— Proton direct ionization (PDI), single event upsets (SEUs), static random access memories (SRAMs).**

NOMENCLATURE

List of Symbols in (1)

Symbols	Remarks	Unit
XS	SEU XS per SRAM bit cell	cm^2/bit
A_{SRAM}	Area of SRAM bit cell	cm^2
r	Ratio of the drift-dominant area to A_{SRAM}	-
ζ	Circuit loading factor (= 2)	-
C_L	Internal load capacitance⋆	fF
d_{fnl}	Funneling-based collection length	nm
d_{diff}	Diffusion-based collection length	nm
V_{DD}	Power supply voltage	V
V_{DR}	Data retention voltage	V
L	LET of incident ions	MeV·cm^2/mg

⋆ C_{load} in [16] is replaced with $5C_L$ after [17].

List of Symbols in (2)–(5)

Symbols	Remarks	Unit
Z_1	Atomic number for the incident particle (Z_1=1 for proton)	-
Z_2	Atomic number for the target material(Z_2=14 for Si)	-
A_2	Mass number of the target material (A_2=28 for Si)	g/mol
β	Relative velocity of the incident particle to the speed of light	-
I	Mean ionization potential ($I = Z_2 \cdot 10$ for Si)	eV
C	Unitless Euler–Mascheroni constant ($C = 2e^{-\gamma}$ with $\gamma = 0.5772$)	-
c	Speed of light	m/s
m_e	Rest mass of the electron (m_e=511/c^2)	keV/(m/s)^2
m_p	Rest mass of the proton (m_p=9.38×10^2/c^2)	MeV/(m/s)^2
α	Unitless fine-structure constant ($\alpha \approx 1/137$)	
p_0	Semi-empirical unitless parameter (p_0=0.774 for proton and Si after [20])	-
p_1	Semi-empirical unitless parameter (p_1=1.231 for proton and Si after [20])	-
ρ	Mass density of the target material	mg/cm^3

Received 1 February 2025; revised 17 March 2025 and 17 April 2025; accepted 6 May 2025. Date of publication 9 May 2025; date of current version 18 August 2025. This work was supported by Japan Aerospace Exploration Agency. *(Corresponding author: K. Takeuchi.)*

K. Takeuchi was with the Department of Informatics, Kyoto University, Kyoto 606-8501, Japan. He is now with Japan Aerospace Exploration Agency, Tsukuba 305-8505, Japan (e-mail: takeuchi.kozo@jaxa.jp).

K. Sakamoto, Y. Tsuchiya, and H. Shindo are with Japan Aerospace Exploration Agency, Tsukuba 305-8505, Japan (e-mail: sakamoto.keita@jaxa.jp).

T. Kato and R. Nakamura are with Socionext Inc., Kawasaki 213-0012, Japan (e-mail: kato.takashi@socionext.com).

A. Takeyama, T. Makino, and T. Ohshima are with the National Institutes for Quantum Science and Technology, Takasaki, Gunma 370-1292, Japan (e-mail: takeyama.akinori@qst.go.jp).

M. Hashimoto is with the Department of Informatics, Kyoto University, Kyoto 606-8501, Japan (e-mail: hashimoto@i.kyoto-u.ac.jp).

Digital Object Identifier 10.1109/TNS.2025.3568455

I. INTRODUCTION

PROTON-INDUCED single event effects (SEEs) on commercial semiconductors are becoming an increasing concern due to the active use of commercial-off-the-shelf (COTS) parts for low-Earth orbit satellites. COTS parts are typically manufactured using highly scaled technology nodes that have less critical charges (Q_c) in their memory cells. COTS parts can be sensitive to protons, which are among the most abundant particles in orbit.

Protons can interact with silicon and other materials in semiconductor devices in two ways: indirect ionization and direct ionization. These interactions and energy transfers to the target material may take place simultaneously and depend on factors such as energy, target materials, and other conditions. In indirect ionization, protons undergo inelastic collisions with nuclei, generating a nuclear reaction that

results in the emission of protons, alpha particles, neutrons, or gamma rays, along with the recoil of a daughter nucleus [1]. In proton direct ionization (PDI), on the other hand, protons create electron–hole pairs along their trajectory by interacting with the valence electrons in the material, similar to other heavy particles. Protons with energies below 10 MeV exhibit almost negligible indirect ionization; instead, they create electron–hole pairs through PDI and vice versa [2]. Due to the PDI effect, where the protons deposit more energy in the materials just before stopping, the cross section (XS) of single event upsets (SEUs) increases for protons below a few megaelectronvolts. According to the stopping and range of ions in matter (SRIM) code [3], the Bragg peak at 55 keV proton energy is approximately 0.54 MeV $\cdot$ cm^2/mg in Si.

A quasi-monoenergetic (QME) low energy proton (LEP) irradiation is often performed to measure PDI XSs directly, whereas a heavily degraded high-energy proton irradiation is also performed both measuring XSs and extracting information on sensitive volume (SV) parameters and Q_c for Monte Carlo simulation.

Historically, Rodbell et al. [4] had demonstrated the upset caused by PDI on 65-nm silicon-on-insulator static random access memories (SRAMs) and latches. Since then, memory elements on 65-nm silicon-on-insulator [5], 65-nm bulk [6], and 45–32-nm bulk [7] have been evaluated. Dodds et al. [8], [9], [10] used heavily degraded high-energy protons to replicate shielded space environments and discussed the upset rate in orbit as well as the mechanism of PDI-induced upset.

In recent studies, SEU XSs from 65- to 16-nm SRAMs have been investigated under both QME LEP and heavily degraded high-energy proton irradiations [11], [12], [13]. Using Monte Carlo simulation with estimated SV parameters combining heavy ion (HI) XS data, upset rates under specific orbital and environmental conditions were calculated and discussed. On the other hand, the QME LEP measurement requires an accurate beam energy profile below a few megaelectronvolts with a narrow energy spectrum under vacuum, and the heavily degraded high-energy proton measurement also suffers from the uncertainties in flux and spectrum measurements [12], which also requires detailed Monte Carlo simulations for beam spectrum reconstruction. In addition, PDI XS data as a function of proton energy are often fit by a second-order polynomial function (e.g., [13]), which is exclusively used for fitting purposes. This approach is not applicable for prediction without experimental PDI XS data.

Our previous study investigated the SEU XS model for bulk planar and fin field-effect transistor (FinFET) SRAMs under alpha and heavier ions irradiation, which is based on the model [14], [15] that reproduces the linear energy transfer (LET) and voltage dependence [16]. Since the LET of a proton is also a metric of the PDI, the proposed model may explain the energy dependence of proton irradiation below a few megaelectronvolt regimes, where the PDI is the dominant energy transfer mechanism. This article presents a method for predicting the XS of SEUs under a few megaelectronvolt protons by processing the SEU XS data obtained under HI irradiation. The applicability of our SEU XS model for the low LET regime is first validated with ^{12}C irradiation results. Then, the XS for PDI is predicted and compared with experimental data.

This article is organized as follows. The details of the proposed method that predicts PDI-induced SEU XSs as a function of proton energy are explained in Section II. Section III describes the HI irradiation including experimental setup for the HI irradiation to compare the proton-equivalent LET, followed by the results and discussion of the method in Section IV.

II. Proposed Method

Based on the model in our previous study [16], the SEU XS of bulk SRAMs is formulated as follows:

$$\mathrm{XS} = A_{\mathrm{SRAM}}\left[r\cdot\exp\left(-\frac{5\zeta C_L}{d_{\mathrm{fnl}}}\frac{V_{\mathrm{DD}}-V_{\mathrm{DR}}}{0.01L}\right) + (1-r)\cdot\exp\left(-\frac{5\zeta C_L}{d_{\mathrm{diff}}}\frac{V_{\mathrm{DD}}-V_{\mathrm{DR}}}{0.01L}\right)\right] \quad (1)$$

where the symbols in (1) are described in Nomenclature.

This work proposes replacing L in (1) with a function of LET, $L(E_p)$ where the proton energy E_p is the argument, and deriving XS as a function of the proton energy. While L is normally considered as the HI-induced LET in (1), it can be translated into proton energy by Bethe's stopping power formula [18], which describes the relationship between the stopping power (identical to L) and the proton energy under given conditions. Note that Bethe's stopping power formula has been corrected and modified by several studies. A semi-empirical analytical model is discussed in [19] and its accuracy is shown in [20] for proton irradiation in Si. The SEU XSs of PDI can be expressed analytically by combining (1) and a semi-empirical analytical model in [20].

Based on (1) and (8) in [20], the semi-empirical LET ($-dE/\rho dx$ or L) formula, expressed in MeV $\cdot$ cm^2/mg, as a function of the incident particle's energy, is given as follows:

$$-\frac{1}{\rho}\frac{dE}{dx} = 3.075\times10^{-4}\times\frac{Z_1^2\cdot Z_2}{A_2\cdot\beta^2}\cdot p_0\cdot\ln\left(1+p_1 C\frac{m_e c^2\beta^3}{Z_1 I\alpha}\cdot\frac{1}{\sqrt{1+\left(\frac{C\beta}{2Z_1\alpha}\right)^2}}\right) \quad (2)$$

where the symbols are described in Nomenclature. Equation (2) is derived by substituting (8) into (1) in [20].

Supposing

$$P_0 = 3.075\times10^{-4}\times\frac{Z_1^2\cdot Z_2}{A_2}\cdot p_0$$

$$P_1 = p_1 C\frac{m_e c^2}{Z_1 I\alpha}$$

and

$$P_2 = \left(\frac{C}{2Z_1\alpha}\right)^2$$

(2) turns to be

$$-\frac{1}{\rho}\frac{dE}{dx} = \frac{P_0}{\beta^2}\cdot\ln\left(1+P_1\beta^3\frac{1}{\sqrt{1+P_2\beta^2}}\right). \tag{3}$$

When $L < 1$ and $d_{\mathrm{fnl}} > d_{\mathrm{diff}}$, (1) can be approximated to be as follows, assuming $L_{e1} = (5\zeta C_L/d_{\mathrm{fnl}})(V_{\mathrm{DD}} - V_{\mathrm{DR}})$:

$$\mathrm{XS} \simeq A_{\mathrm{SRAM}}\cdot r\cdot\exp\left(-\frac{L_{e1}}{0.01L}\right). \tag{4}$$

Using the non-relativistic relationship between the proton energy (E_p), velocity (v), and rest mass of the proton (m_p), $E_p = m_p v^2/2$, when the proton energy is below a few megaelectronvolts, an analytical expression for PDI-induced XS as a function of proton energy is then derived by combining (3) and (4) as follows:

$$\mathrm{XS}(E_p) \simeq A_{\mathrm{SRAM}}\cdot r\cdot\exp\left(-\frac{L_{e1}}{0.01}\cdot\frac{\frac{2E_p}{m_pc^2}}{P_0\cdot\ln\left(1+P_1\left(\frac{2E_p}{m_pc^2}\right)^{\frac{3}{2}}\cdot\frac{1}{\sqrt{1+P_2\frac{2E_p}{m_pc^2}}}\right)}\right). \tag{5}$$

The above equation describes the relation between the proton energy E_p and XS and can be used to predict SEU XSs of PDI.

III. Low LET HI Irradiation

This section examines the applicability of the proposed model to the low LET region through the irradiation of HIs with the proton-equivalent low LET.

A. Experimental Setup

The device under test (DUT) is an SRAM fabricated by a commercial 16-nm bulk FinFET process. The package was decapped before irradiation. A 5.5 Mb of SRAM macros embedded in the DUT were evaluated under HI irradiation. The details of the evaluation method, including the measurement of V_{DR} and the calculation of event-based XSs, are described in [21] and [22]. Unless otherwise specified in this article, "cross section" or "XS" refers to this event-based XS.

The HI-induced SEUs of the DUT were evaluated using the cyclotron at the Takasaki Ion Accelerators for Advanced Radiation Application (TIARA) of the National Institutes for Quantum Science and Technology (QST). The DUT was irradiated with a mono-energetic carbon (^{12}C) beam in a vacuum chamber. The LET and the travel range in Si were calculated by the SRIM and transport of ions in matter (TRIM) code [3] and are listed with related information, including the LET value after penetrating the back-end-of-line (BEOL), in Table I. The thickness of the BEOL was assumed to be approximately 10 μm based on our previous study [21]. In this case, there is no difference in the LET value before and after penetrating the BEOL. The LET value of ^{12}C in Si is comparable to that of protons at the Bragg peak. The DUT was irradiated at room temperature with normal incidence to the chip under a nominal V_{DD} condition of 0.8 V.

TABLE I
Irradiation Conditions

Ion	Energy (MeV)	LET at chip surface (MeV·cm^2/mg)	LET after BEOL (MeV·cm^2/mg)	Range (μm)
^{12}C	320	0.576	0.576	1345

TABLE II
Model Parameters Calibrated by the Alpha Irradiation Results of DUT [16]

Parameters	Value	Unit	Calibrated
L	0.85	MeV·cm^2/mg	No (Fixed)
V_{DD}	-	V	No (Variable)
V_{DR}	0.15	V	No (Fixed)
A_{SRAM}	9×10^{-10}	cm^2/bit	No (Fixed)
$C_{\mathrm{L}}^{\dagger}$	0.52	fF	No (Fixed)
d_{fnl}	95.7	nm	Yes
d_{diff}	32.8	nm	Yes
r	0.258	-	Yes

† C_{L} is estimated from Q_{c} based on the value reported in [23]. (See Table. VII for the detail.)

B. Results and Discussion for HI Irradiation

Fig. 1 shows the comparison of the predicted XS curve (black line) as a function of LET with the experimental results (a black circle for ^{12}C). The curve was predicted using (1) and the parameters in Table II. The gray circles show the experimental results from [21], of which LETs were recalculated after penetrating the BEOL. Fig. 1 demonstrates the accurate prediction of XSs for both high LET ions (gray circles) and the low LET ion (^{12}C). The LET values before and after penetrating the BEOL are listed in Table III. The LET values after penetrating the BEOL are calculated by the SRIM/TRIM code based on the metal and insulator layers of a similar manufacturing process.

Note that the parameters of (1) were calibrated by fitting them to the results of alpha irradiation under various V_{DD} conditions [16], and the calibrated parameters are listed in Table II. The essential unknown parameters to be determined in (1) are: A_{SRAM}, r, $\zeta C_L/d_{\mathrm{fnl}}$, and $\zeta C_L/d_{\mathrm{diff}}$. According to [14], the circuit loading factor ζ is approximately equal to two, and this value is applicable across a wide range of technology generations. A_{SRAM}, representing the SRAM bit cell area, can be obtained from the existing literature. Assuming a fixed value of C_L, the number of parameters requiring calibration is reduced to three: r, d_{fnl}, and d_{diff} [16]. The value of C_L is assumed as a realistic value based on Q_c reported in the literature [23]. Here, "calibration" and "calibrate" refer to determining these three parameter values through curve fitting.

In Fig. 1, the gray dotted and the gray solid lines represent the cumulative Weibull distribution (known as the Weibull curve [24]) and the cumulative log-normal distribution (known

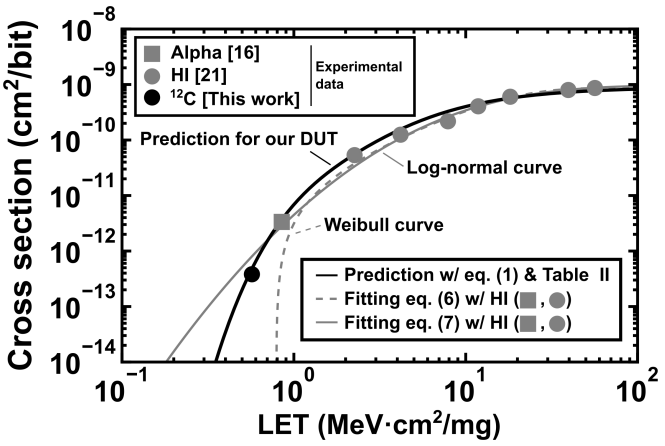

Fig. 1. Comparison of the predicted XS curve as a function of LET with the experimental results. The black circle shows the XS under ^{12}C irradiation at 0.8 V condition. The gray square represents the XS under alpha irradiation. The black line shows the prediction using (1) and the parameters in Table II. The parameters in Table II were calibrated using data from alpha irradiation under various V_{DD} conditions. The gray circles also show the XSs of various HIs. The parameters of (1) and the experimental results except for ^{12}C are obtained from [16] and [21] of which LET is converted to the values after penetrating the BEOL. The gray dotted line and the solid line represent the Weibull and log-normal curves, respectively, fit using alpha and HI experimental data.

TABLE III
LIST OF LET CONVERTED TO THE VALUE AFTER PENETRATING THE BEOL

Ions	Energy (MeV)	LET at chip surface (MeV·cm^2/mg)	LET after BEOL (MeV·cm^2/mg)
^{129}Xe	454	68.9	56.4
^{84}Kr	322	40.3	39.5
^{40}Ar	150	15.8	18.2
^{40}Ar	330	11.0	11.8
^{20}Ne	75	6.5	7.88
^{15}N	56	3.6	4.18
^{10}B	37	1.9	2.26
^{4}He	5.4	0.58	0.85

as the log-normal curve [25], [26]), respectively. They are fit to the alpha [16] and HI [21] experimental data using (6) and (7). The Weibull curve is formulated as follows:

$$\mathrm{XS} = \mathrm{XS_{sat}}\left[1 - \exp\left\{-\left(\frac{L - L_T}{W}\right)^S\right\}\right] \tag{6}$$

where $\mathrm{XS_{sat}}$, L_T, W, and S are the saturated XS, threshold LET, width parameter, and dimensionless exponent, respectively.

The log-normal curve is formulated as follows:

$$\mathrm{XS} = \mathrm{XS_{sat}}\left[\frac{1}{2}\mathrm{erfc}\left(-\frac{\ln(L) - m}{\sqrt{2}s}\right)\right] \tag{7}$$

where erfc, m, and s represent the complementary error function, mean of the log-normal function, and standard deviation of the log-normal function, respectively. The best-fit values of Weibull and log-normal curves are listed in Table IV. All the fittings were performed using the same dataset from [13] and [27] and the non-linear least-squares minimization and curve-fitting method in Python (lmfit) [28].

TABLE IV
BEST-FIT VALUES OF THE WEIBULL AND LOG-NORMAL CURVES

Curves	Parameters	Value	Unit
Weibull	XS_{sat}	8.67×10^{-10}	cm^2/bit
	L_T	0.789	MeV·cm^2/mg
	W	16.1	MeV·cm^2/mg
	S	1.30	-
Log-normal	XS_{sat}	9.68×10^{-10}	cm^2/bit
	m	14.8	-
	s	1.03	-

TABLE V
MODEL PARAMETERS CALIBRATED BY THE RESULTS OF THE 16-nm SRAMS [13], [27]

Parameters	Value	Unit	Calibrated	Remarks
L	-	MeV·cm^2/mg	No (Variable)	-
V_{DD}	0.8	V	No (Fixed)	[16]
V_{DR}	0.15	V	No (Fixed)	[16]
A_{SRAM}	7.4×10^{-10}	cm^2/bit	No (Fixed)	[30]
$C_L^{\dagger}$	0.52	fF	No (Fixed)	[23]
d_{fnl}	129.5	nm	Yes	-
d_{diff}	12.6	nm	Yes	-
r	0.0822	-	Yes	-

† C_L is estimated from Q_c based on the value reported in [23]. (See Table. VII for the detail.)

The Weibull curve, indicating no SEU below 0.7 MeV · cm^2/mg, demonstrates its limitations for extrapolation and prediction in the low LET region. The log-normal curve overestimates the XS below 0.7 MeV · cm^2/mg. It should be noted that (1) consists entirely of physics-based parameters, allowing XS to be predicted without the need for a full set of HI results, unlike the Weibull and log-normal curves. Despite anticipated differences between the HI-induced LET and the proton-induced LET, Fig. 1 suggests that the proposed method could apply to predicting the PDI effect.

IV. PREDICTION OF PDI-INDUCED SEU XS

In this section, PDI experimental data for two types of SRAMs, fabricated using 16-nm bulk FinFET and 40-nm bulk planar processes, are evaluated using the proposed method. The data were obtained from the literature using the plot digitization program [29].

A. 16-nm FinFET SRAMs

Fig. 2 shows the XS fitting results of 16-nm SRAMs [13], [27] and our DUT discussed in Section III. Since the HI experimental data are different from that of our DUT despite the same 16-nm process, the high density (HD) SRAMs are assumed. The parameters calibrated by the experimental data of 16-nm SRAMs are listed in Table V. According to the fitting results, our DUT and the 16-nm SRAMs have similar SEU XSs for PDI, as shown in Fig. 2. Note that due to the lack of experimental data below 1 MeV · cm^2/mg for the fitting, there would be some uncertainty in this region.

Fig. 3 shows the predicted XS curve for the PDI of the 16-nm SRAMs based on the method described in Section II

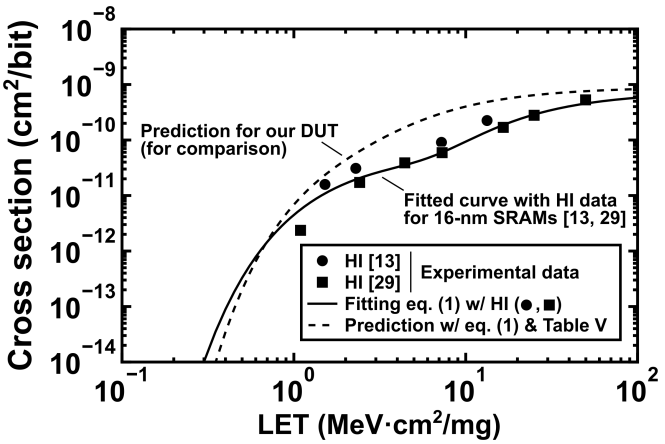

Fig. 2. XS fitting results of the 16-nm bulk SRAMs. The black circles and squares represent the HI irradiation experimental data. The experimental data are obtained from [13] and [27]. The black solid line shows the fit curve to the data in [13] and [27]. The black dotted line shows the prediction of our DUT for comparison, which is identical to the black line in Fig. 1.

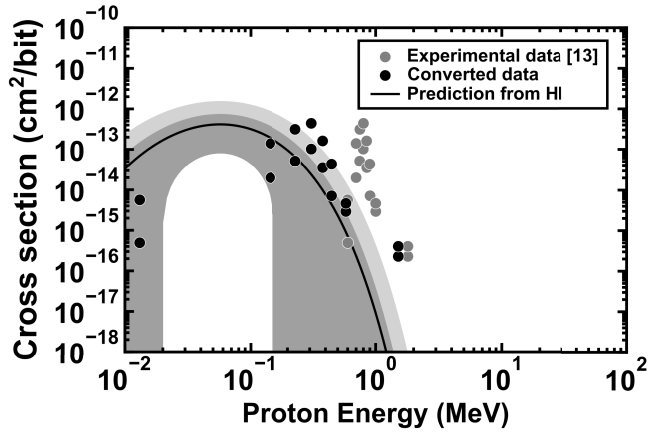

Fig. 3. Predicted XS curve as a function of the incident proton energy. The black solid line predicts the PDI SEU XS of the 16-nm SRAMs in [13] and [27]. The dark gray shaded area shows the $\pm 1\sigma$ confidence interval band of the predicted curve. The light gray shaded area represents the LET error bar, taking into account a 20% overshoot of the experimental LET [31], [32]. The gray circles show the experimental data of SEU XSs under QME LEP irradiation (obtained from [13]). The black circles show the SEU XSs of the same data, where the proton energy is converted to the equivalent values after penetrating the BEOL.

and the QME LEP experimental data [13]. The dark gray shaded area shows the $\pm 1\sigma$ confidence interval band of the predicted curve. Due to the lack of the HI experimental data below 1 MeV · cm^2/mg for the parameter calibration, the confidence interval of the parameters widens in this region. The confidence intervals were calculated using partial differentiation of the model and the covariance matrix, as discussed in [33], through the lmfit [28].

According to [31] and [32], the experimental values of proton LET in Si may vary by as much as 20% larger compared to the estimated values obtained using (2). The light gray shaded area in Fig. 3 represents the LET error bar, considering an overshoot in LET variation from the experimental database [31], [32].

In Fig. 3, the gray circles represent the experimental SEU XSs under LEP irradiation [13], while the black circles indicate the SEU XSs where the proton energy is converted to the equivalent values after penetrating the BEOL. The predicted curve correctly reproduces the unimodal trend as proton energy decreases. While the peak position and the shape of the curve in the energy axis are slightly different even after the conversion of the LEP experimental data, the peak value of XS is comparable between the predicted and experimental data. The differences in peak position and shape might be caused by the straggling of the LEP in the BEOL, which results in some protons arriving at the SRAMs at an angle other than the normal angle of incidence, as well as a broadening of the proton energy spectrum. Note that there are uncertainties in the LEP experimental data [13] as well, likely due to sample-to-sample variation.

For the conversion, the copper (Cu) and the porous carbon-incorporated silicon oxide (SiOC) layers are assumed to be 6 μm thick, because 600 keV protons can penetrate the BEOL layers in the experimental data [13]. While this value is relatively thin in these manufacturing generations, the same value was assumed in the previous study by the same group [34]. It is worth mentioning that slight differences in the assumed BEOL thickness may lead to variations in the converted experimental data. The BEOL layer information [30] and the material property of SiOC [35] are used to construct the BEOL layers in the TRIM code.

B. 40-nm Bulk SRAMs

Fig. 4 shows the XS fitting results of 40-nm bulk SRAMs. While the experimental data have deviations in the literature, (1) could fit data with a wide range of LETs. The parameters calibrated by the experimental data of 40-nm SRAMs are listed in Table VI. Since the value of V_{DR} could not be obtained from the literature, the value of 25% V_{DD} is assumed. While this may result in a loss of accuracy for the V_{DD} dependence, it is not expected to affect the predictions at nominal V_{DD}.

Fig. 5 shows the predicted XS curve for the 40-nm bulk SRAMs and the QME LEP experimental data [12], [13]. The black solid line and the gray shaded area accurately predict the experimental data, where the proton energy is converted to the equivalent values after penetrating the BEOL. For the conversion, Cu and porous SiOC layers are assumed to be approximately 4 μm thick, taking into account the fact that 450 keV protons can penetrate the BEOL layers. These relatively thin BEOL layers could contribute to the accurate agreement between the prediction and the converted experimental data. The BEOL layer information from a similar process [36] is used to construct the BEOL layers in the TRIM code.

C. Physical Insights of Parameters

The model parameters, calibrated by fitting to the HI experimental data, may provide insights into the characteristics of actual SRAM bit cells, as all the parameters have physical units, unlike those in the Weibull and log-normal curves.

Table VII lists model parameters calibrated in this article. The values of d_{fnl} can be interpreted as the depth of the drift

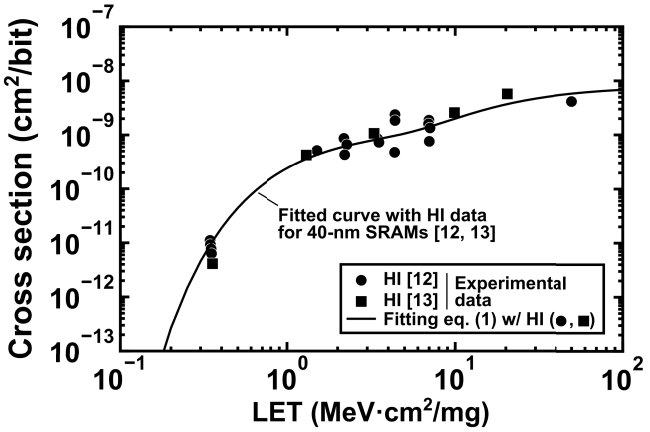

Fig. 4. XS fitting results of the 40-nm bulk SRAMs. The black circles and squares represent the HI irradiation experimental data. The black solid line shows the fit curve for the HI data. The experimental data are obtained from [12] and [13]).

TABLE VI
MODEL PARAMETERS CALIBRATED BY THE RESULTS OF THE 40-nm SRAMS [11], [12]

Parameters	Value	Unit	Calibrated	Remarks
L	-	MeV·cm^2/mg	No (Variable)	-
V_{DD}	1.1	V	No (Fixed)	[11]
V_{DR}	0.275	V	No (Fixed)	25% of V_{DD}
A_{SRAM}	8.11×10^{-9}	cm^2/bit	No (Fixed)	[12]
$C_L^{\dagger}$	0.32	fF	No (Fixed)	[23]
d_{fnl}	155	nm	Yes	-
d_{diff}	13.0	nm	Yes	-
r	0.164	-	Yes	-

† C_L is estimated from Q_c based on the value reported in [23]. (See Table. VII for the detail.)

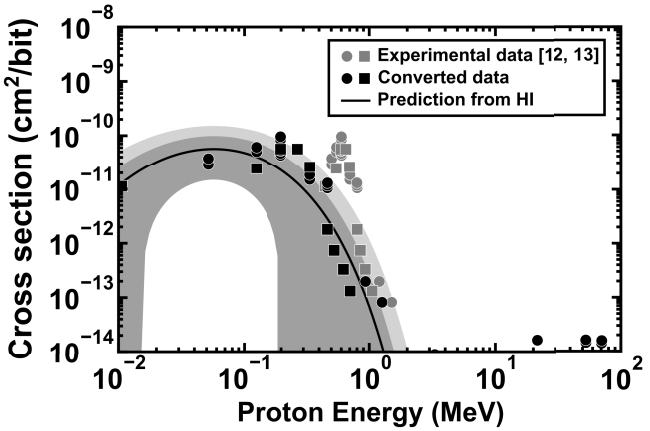

Fig. 5. Predicted XS curve as a function of the incident proton energy. The black solid line predicts the PDI SEU XS of the 40-nm bulk SRAMs in [12] and [13]. The dark gray shaded area shows the $\pm1\sigma$ confidence interval band of the predicted curve. The light gray shaded area represents the LET error bar, taking into account a 20% overshoot of the experimental LET [31], [32]. The gray circles and squares show the SEU XSs under QME LEP irradiation (obtained from [12] and [13]). The black circles and squares show the SEU XSs of the same data, where the proton energy is converted to the equivalent values after penetrating the BEOL.

charge collection component. For 16-nm SRAMs, values of 95.7 and 129.5 nm correspond to the fin height [37], whereas the value of 155 nm for 40-nm SRAMs aligns with the range

TABLE VII
SUMMARY OF MODEL PARAMETERS CALIBRATED BY THE RESULTS OF OUR DUT, THE 16-nm, AND THE 40-nm SRAM

Parameters	Our DUT (16-nm)	16-nm	40-nm	Unit
Q_c [23] (=$2C_LV_{DD}$)	0.71-0.83		0.71	fC
C_L from Q_c	0.52		0.32	fF
V_{DD}	0.8	0.8	1.1	V
V_{DR}	0.15	0.15	0.275	V
A_{SRAM}	9×10^{-10}	7.4×10^{-10}	8.11×10^{-9}	cm^2/bit
C_L	0.52	0.52	0.32	fF
d_{fnl}	95.7	129.5	155	nm
d_{diff}	32.8	12.6	13.0	nm
r	0.258	0.0822	0.164	-

of the shallow trench isolation (STI) depth in the similar technology node [38].

The values of d_{diff} represent the depth for the diffusion charge collection component. According to [39], the diffusion charge collection length in modern devices ranges approximately from 10 to 100 nm. These values are consistent with our results.

The values of r could offer insights into the ratio of the drift charge collection component, providing information about actual SRAM bit cells. With reasonable assumptions, we can extract values of active area width (W_{drift}) related to the drift charge collection from r (see the Appendix for details). W_{drift} of our DUTs, 16-nm SRAMs, and 40-nm SRAMs are calculated as 51.6, 22.5, and 88.7 nm, respectively. They are comparable with the width of fin, sub-fin [37], or transistors [40] in the SRAM bit cell. Note that the track radius of the incident ion might affect W_{drift} (and r) in the highly scaled manufacturing process such as the FinFET process.

These findings suggest that physical analysis and the extraction of dimensions could facilitate a straightforward prediction of PDI XSs. While the parameters in (1) could potentially be used directly to describe multiple SVs for both drift and diffusion charge collection, further research is needed to interpret these parameters as characteristics of actual SRAM bit cells across the various generations of SRAMs.

D. Simple Conversion for an Approximate Prediction

In Sections IV-A and IV-B, the QME LEP experimental data were converted to the values where the proton energy is the equivalent value after penetrating the BEOL using the TRIM code. In contrast, the predicted curve can also be converted to the approximate values of the proton energy before penetrating the BEOL for ease of use and for approximate prediction.

Figs. 6 and 7 show the conversion results for 16- and 40-nm data, respectively. The black solid lines are linearly shifted by 0.6 and 0.45 MeV, respectively, in the positive direction from the original predictions (the black dashed lines) based on the thicknesses of the BEOL layers. A 0.6 and 0.45 MeV shift in proton energy corresponds to an approximate conversion of 6 and 4 μm of BEOL thickness, respectively. This simple conversion works well, and the shifted curves roughly predict

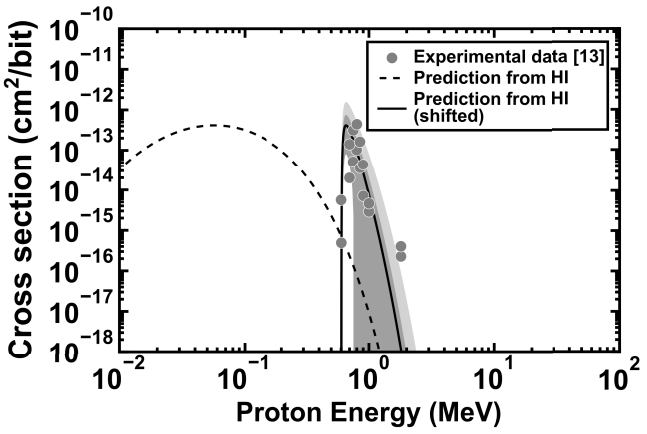

Fig. 6. Predicted XS curve as a function of the incident proton energy. The black dashed line predicts the PDI SEU XS of the 16-nm SRAMs in [13] and the black solid line is shifted by 600 keV (0.6 MeV). The dark and light gray shaded areas show the $\pm 1\sigma$ confidence interval band of the predicted curve and the LET error bar, respectively, both shifted by 0.6 MeV. The gray circles show the SEU XSs under QME LEP irradiation (obtained from [13]).

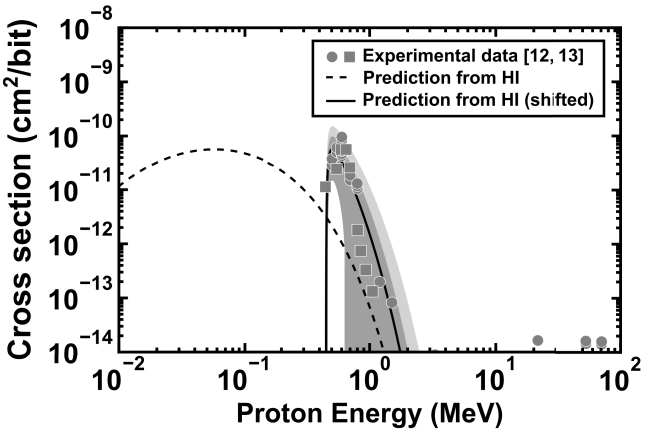

Fig. 7. Predicted XS curve as a function of the incident proton energy. The black dashed line predicts the PDI SEU XS of the 40-nm SRAMs in [12] and [13], and the black solid line is shifted by 450 keV (0.45 MeV). The dark and light gray shaded areas show the $\pm 1\sigma$ confidence interval band of the predicted curve and the LET error bar, respectively, both shifted by 0.45 MeV. The gray circles and squares show the SEU XSs under QME LEP irradiation (obtained from [12] and [13]).

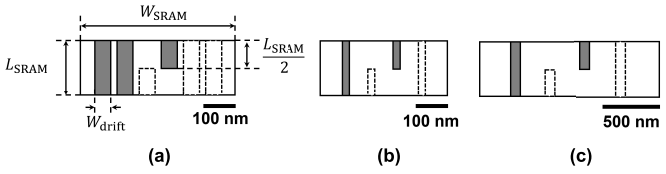

Fig. 8. Conceptual illustrations of the SRAM bit cell for calculating W_{drift}. (a) Our DUT. (b) 16-nm SRAM. (c) 40-nm SRAM. The gray hatched boxes represent the OFF-state n- and p-type transistors.

the experimental data, as shown in Figs. 6 and 7. This simple conversion can be used to consider the fluence, flux, and proton energy when performing QME LEP irradiation.

For the prediction for advanced nodes, the BEOL stack information from the literature (such as [41], [42]) might be utilized. Even if the thickness of the BEOL stack for a given process is not available, it can be assumed to range from 4 to 10 μm. This allows us to provide a prediction interval. Note that this conversion is not physically accurate and is intended only for approximate prediction. While the linear shifting approximation presented in this article provides predictions easily and with sufficient accuracy, as shown in Figs. 6 and 7, be reminded that it may also introduce artifacts that could potentially lead to misunderstandings of the experimental data.

TABLE VIII
SUMMARY OF W_{drift} OF OUR DUT, THE 16-nm, AND THE 40-nm SRAMS

Parameters	Our DUT (16-nm)	16-nm	40-nm	Unit
A_{SRAM}	9×10^{-10}	7.4×10^{-10}	8.11×10^{-9}	cm^2/bit
r	0.258	0.0822	0.164	-
L_{SRAM}	180 [22]	180 [22]	500 [40]	nm
W_{SRAM}	500 [22]	411	1622	nm
W_{drift}	51.6	22.5	88.7	nm

V. CONCLUSION

The method for predicting PDI-induced SEU XS has been presented in this article. Using our model fit to the experimental HI data, SEU XSs induced by PDI are adequately predicted for both 16-nm FinFET and 40-nm bulk SRAMs when the proton energy is converted to the equivalent values after penetrating the BEOL. By shifting 0.45–0.6 MeV in the positive direction from the original prediction based on the thicknesses of the BEOL layers, the approximate prediction can also be easily compared with the QME LEP experimental data.

APPENDIX
ESTIMATION OF W_{drift} FROM CALIBRATED r

Since r is the ratio of the drift-dominant area to A_{SRAM}, $A_{SRAM} \times r$ is the drift-dominant area from the top view on the SRAM. The W_{drift} value of each SRAM is calculated as follows, where W_{drift} will be given below.

1) Assume that the OFF-state transistors in the SRAM bit cell as the drift-dominant area from the top view, as shown in Fig. 8.
2) Define L_{SRAM}, W_{SRAM}, and W_{drift} as the length, width of the SRAM, and the drift-dominant area width, respectively, as shown in Fig. 8.
3) For the 2-fin SRAMs (our DUTs), W_{SRAM} is calculated as (A2) by solving (A1).
4) For the 1-fin 16-nm SRAMs and 40-nm SRAMs, W_{SRAM} is calculated as (A4) by solving (A3).

Table VIII summarized W_{drift} and other parameters. Fig. 8 shows the illustrations of the SRAM bit cell for calculating W_{drift}

$$A_{SRAM} \times r = 2 \times W_{drift} \times L_{SRAM} + W_{drift} \times \frac{1}{2} L_{SRAM} \quad \text{(A1)}$$

$$W_{drift} = \frac{2}{5} \frac{A_{SRAM} \times r}{L_{SRAM}} \quad \text{(A2)}$$

$$A_{SRAM} \times r = W_{drift} \times L_{SRAM} + W_{drift} \times \frac{1}{2} L_{SRAM} \quad \text{(A3)}$$

$$W_{drift} = \frac{2}{3} \frac{A_{SRAM} \times r}{L_{SRAM}}. \quad \text{(A4)}$$

REFERENCES

[1] R. C. Lacoe, "CMOS scaling, design principles and hardening-by design methodologies," in *Proc. IEEE NSREC Short Course*, 2003, ch. 2, pp. 1–142.

[2] R. Reed, "Fundamental mechanisms for single particle-induced soft errors," in *Proc. IEEE NSREC Short Course*, 2008, sec. 1, pp. 1–63.

[3] J. F. Ziegler. (2013). *SRIM—The Stopping and Range of Ions in Matter*. [Online]. Available: http://www.srim.org/

[4] K. P. Rodbell, D. F. Heidel, H. H. K. Tang, M. S. Gordon, P. Oldiges, and C. E. Murray, "Low-energy proton-induced single-event-upsets in 65 nm node, silicon-on-insulator, latches and memory cells," *IEEE Trans. Nucl. Sci.*, vol. 54, no. 6, pp. 2474–2479, Dec. 2007.

[5] D. F. Heidel et al., "Low energy proton single-event-upset test results on 65 nm SOI SRAM," *IEEE Trans. Nucl. Sci.*, vol. 55, no. 6, pp. 3394–3400, Dec. 2008.

[6] B. D. Sierawski et al., "Impact of low-energy proton induced upsets on test methods and rate predictions," *IEEE Trans. Nucl. Sci.*, vol. 56, no. 6, pp. 3085–3092, Dec. 2009.

[7] N. Seifert, B. Gill, J. A. Pellish, P. W. Marshall, and K. A. LaBel, "The susceptibility of 45 and 32 nm bulk CMOS latches to low-energy protons," *IEEE Trans. Nucl. Sci.*, vol. 58, no. 6, pp. 2711–2718, Dec. 2011.

[8] N. A. Dodds et al., "Hardness assurance for proton direct ionization-induced SEEs using a high-energy proton beam," *IEEE Trans. Nucl. Sci.*, vol. 61, no. 6, pp. 2904–2914, Dec. 2014.

[9] N. A. Dodds et al., "The contribution of low-energy protons to the total on-orbit SEU rate," *IEEE Trans. Nucl. Sci.*, vol. 62, no. 6, pp. 2440–2451, Dec. 2015.

[10] N. A. Dodds et al., "New insights gained on mechanisms of low-energy proton-induced SEUs by minimizing energy straggle," *IEEE Trans. Nucl. Sci.*, vol. 62, no. 6, pp. 2822–2829, Dec. 2015.

[11] A. Coronetti et al., "Assessment of proton direct ionization for the radiation hardness assurance of deep submicron SRAMs used in space applications," *IEEE Trans. Nucl. Sci.*, vol. 68, no. 5, pp. 937–948, May 2021.

[12] S. Lüdeke et al., "Proton direct ionization in sub-micron technologies: Test methodologies and modeling," *IEEE Trans. Nucl. Sci.*, vol. 70, no. 4, pp. 667–677, Apr. 2023.

[13] M. Glorieux et al., "Methods for proton direct ionization SEU characterization and orbital error-rate estimation," *IEEE Trans. Nucl. Sci.*, vol. 71, no. 8, pp. 1707–1714, Aug. 2024.

[14] D. Kobayashi et al., "An SRAM SEU cross section curve physics model," *IEEE Trans. Nucl. Sci.*, vol. 69, no. 3, pp. 232–240, Mar. 2022.

[15] L. D. Edmonds, "SEU cross sections derived from a diffusion analysis," *IEEE Trans. Nucl. Sci.*, vol. 43, no. 6, pp. 3207–3217, Dec. 1996.

[16] K. Takeuchi, T. Kato, and M. Hashimoto, "An SEU cross section model reproducing LET and voltage dependence in bulk planar and FinFET SRAMs," in *Proc. IEEE Int. Rel. Phys. Symp. (IRPS)*, Apr. 2024, pp. 636–639.

[17] D. Kobayashi, M. Uematsu, and K. Hirose, "Threshold and characteristic LETs in SRAM SEU cross section curves," *IEEE Trans. Nucl. Sci.*, vol. 70, no. 4, pp. 707–713, Apr. 2023.

[18] G. Knoll, *Radiation Detection and Measurement*, 4th ed., Hoboken, NJ, USA: Wiley, Sep. 2010.

[19] L. de Ferrariis and N. R. Arista, "Classical and quantum-mechanical treatments of the energy loss of charged particles in dilute plasmas," *Phys. Rev. A, Gen. Phys.*, vol. 29, no. 4, pp. 2145–2159, Apr. 1984.

[20] S. Lüdeke and A. Javanainen, "Proton direct ionization in sub-micron technologies: Numerical method for RPP parameter extraction," *IEEE Trans. Nucl. Sci.*, vol. 69, no. 3, pp. 254–263, Mar. 2022.

[21] K. Takeuchi et al., "Voltage dependence of single-event cross sections of FinFET SRAMs for low LET condition," *IEEE Trans. Nucl. Sci.*, vol. 70, no. 8, pp. 1755–1759, Aug. 2023.

[22] K. Takeuchi et al., "Characteristic charge collection mechanism observed in FinFET SRAM cells," *IEEE Trans. Nucl. Sci.*, vol. 69, no. 8, pp. 1833–1839, Aug. 2022.

[23] D. Kobayashi, "Scaling trends of digital single-event effects: A survey of SEU and SET parameters and comparison with transistor performance," *IEEE Trans. Nucl. Sci.*, vol. 68, no. 2, pp. 124–148, Feb. 2021.

[24] E. L. Petersen, J. C. Pickel, J. H. Adams, and E. C. Smith, "Rate prediction for single event effects-a critique," *IEEE Trans. Nucl. Sci.*, vol. 39, no. 6, pp. 1577–1599, Dec. 1992.

[25] E. Petersen, "Cross section measurements and upset rate calculations," *IEEE Trans. Nucl. Sci.*, vol. 43, no. 6, pp. 2805–2813, Dec. 1996.

[26] E. L. Petersen, "Parametric and threshold studies of single event sensitivity," *IEEE Trans. Nucl. Sci.*, vol. 54, no. 4, pp. 1392–1405, Aug. 2007.

[27] N. Tam et al., "Multi-cell soft errors at the 16-nm FinFET technology node," in *Proc. IEEE Int. Rel. Phys. Symp.*, Monterey, CA, USA, Apr. 2015, pp. 4B.3.1–4B.3.5.

[28] M. Newville et al., Jul. 2024, "lmfit/lmfit-py: 1.3.2," *Zenodo*. [Online]. Available: https://doi.org/10.5281/zenodo.12785036

[29] A. Rohatgi. (2023). *WebPlotDigitizer: HTML5 Based Online Tool to Extract Numerical Data From Plot Images*. [Online]. Available: https://github.com/automeris-io/WebPlotDigitizer

[30] S.-Y. Wu et al., "A 16nm FinFET CMOS technology for mobile SoC and computing applications," in *IEDM Tech. Dig.*, Washington, DC, USA, Dec. 2013, pp. 9.1.1–9.1.4.

[31] C. C. Montanari, P. Dimitriou, L. Marian, A. M. P. Mendez, J. P. Peralta, and F. Bivort-Haiek, "The IAEA electronic stopping power database: Modernization, review, and analysis of the existing experimental data," *Nucl. Instrum. Methods Phys. Res. B, Beam Interact. Mater. At.*, vol. 551, Jun. 2024, Art. no. 165336. [Online]. Available: https://www.sciencedirect.com/science/article/pii/S0168583X2400106X

[32] International Atomic Energy Agency (IAEA). (2024). *Stopping Power Database, Version 2024-11*. Accessed: Jan. 17, 2025. [Online]. Available: https://nds.iaea.org/stopping

[33] J. Wolberg, *Data Analysis Using the Method of Least Squares: Extracting the Most Information From Experiments*, 1st ed., Berlin, Germany: Springer, Feb. 2006.

[34] L. Artola et al., "Investigation of the impact of angles and rotation of low-energy protons in SRAM cells down to 16 nm," *IEEE Trans. Nucl. Sci.*, vol. 71, no. 4, pp. 542–547, Jan. 2024.

[35] H.-J. Lee et al., "Structural characterization of porous low-k SiOC thin films using X-ray porosimetry," in *Proc. IEEE Int. Interconnect Technol. Conf.*, Burlingame, CA, USA, Jun. 2002, pp. 54–56.

[36] K. Mistry et al., "A 45 nm logic technology with high-k+metal gate transistors, strained silicon, 9 Cu interconnect layers, 193 nm dry patterning, and 100% pb-free packaging," in *IEDM Tech. Dig.*, Washington, DC, USA, Dec. 2007, pp. 247–250.

[37] D. James, "Moore's Law continues into the 1x-nm era," in *Proc. 27th Annu. SEMI Adv. Semiconductor Manuf. Conf. (ASMC)*, Saratoga Springs, NY, USA, May 2016, pp. 324–329.

[38] E. Josse et al., "A cost-effective low power platform for the 45-nm technology node," in *IEDM Tech. Dig.*, San Francisco, CA, USA, Dec. 2006, pp. 1–4.

[39] J.-L. Autran and D. Munteanu, "Physics-based analytical formulation of the soft error rate in CMOS circuits," *IEEE Trans. Nucl. Sci.*, vol. 70, no. 5, pp. 782–791, May 2023.

[40] NEC Corporation. (2009). *40 nm Node CMOS Platform 'UX8'*. Accessed: Jan. 19, 2025. [Online]. Available: https://www.nec.com/en/global/techrep/journal/g09/n01/pdf/090113.pdf

[41] M. Lofrano et al., "Towards accurate temperature prediction in BEOL for reliability assessment (invited)," in *Proc. IEEE Int. Rel. Phys. Symp. (IRPS)*, Monterey, CA, USA, Mar. 2023, pp. 1005–1011.

[42] B. Sell et al., "Intel 4 CMOS technology featuring advanced FinFET transistors optimized for high density and high-performance computing," in *Proc. IEEE Symp. VLSI Technol. Circuits (VLSI Technol. Circuits)*, Honolulu, HI, USA, Jun. 2022, pp. 282–283.